Advanced FDTD Subgridding: A High-Efficiency Algorithm Leveraging Model Order Reduction for Arbitrary Grid Refinement Ratios

Xinyue Zhang
Department of Electronic Engineering, Maynooth University, Maynooth, Ireland

Abstract

This study introduces an advanced algorithm for Finite-Difference Time-Domain (FDTD) subgridding, enhancing efficiency through model order reduction, adaptable to any grid refinement ratio. The algorithm overcomes traditional FDTD limitations in handling complex geometries, particularly those requiring varied spatial resolutions. By integrating model order reduction, our approach not only maintains computational accuracy but also significantly reduces the computational cost, regardless of the grid refinement ratio. This development represents a substantial leap in electromagnetic simulation, offering a versatile and efficient solution for diverse and complex modeling scenarios.

1 Introduction

The Finite-Difference Time-Domain (FDTD) method is one of the most widely used techniques in electromagnetic simulation. The use of the staggered leap-frog update of electric and magnetic fields makes FDTD a simple and computationally efficient method. However, the main constraint of standard FDTD method is the Courant-Friedrichs-Lewy (CFL) stability condition [1], especially when fine geometrical details exist in the investigated structure. To fully discretize a complicated object, a high spatial resolution is required. The increase of spatial resolution can lead to the decrease of the iteration time step, which will increase the computational cost.

In order to mitigate the computational cost issue, FDTD subgridding was often used [2, 3]. However, FDTD subgridding will involve a higher number of variables and also be constrained by CFL limit of the finest grid in order to preserve stability. Therefore, method of model order reduction was applied on the fine grid in FDTD subgridding to further reduce computational cost [4, 5]. In [6], an impedance transfer function formulation for reduced-order macromodels for FDTD subgridding was proposed. Nevertheless, stability of those approaches was not fully analyzed and guaranteed.

In [7], the reduced-order model of the fine grid was embedded into the main coarse grid with an extended CFL limit. It has been proved to be stable using an dissipative argument. The main drawback of [7] is that the size of the reduced-order model grows linearly with the grid refinement ratio between the coarse and fine grid.

Therefore, a new scheme of model order reduction for FDTD subgridding is proposed in this paper. The fine grid is first merged with a linear interpolation rule. Then method of model order reduction is applied on the coupled system. Finally, the reduced-order model is incorporated into the main coarse region with an extended CFL limit. Compared to the previous work, the reduced model order of the proposed method becomes independent of the grid refinement ratio. The size of the reduced model is much lower and the computational cost is significantly reduced.

2 Proposed Scheme

In a multiscale scenario of FDTD simulation, a transverse-electric mode with field components E_x, E_y and H_z is considered. There exists at least one fine region that is refined with a fine mesh and the rest of the region is discretized with a coarse mesh. The x-directed and y-directed cell length of each coarse grid are Δx and Δy. The discretization of the refined region is $\Delta\hat{x}$ and $\Delta\hat{y}$. The grid refinement ratio between coarse and fine grid is defined as r. The entire system can be considered as the connection of three subsystems: the coarse grid, the fine mesh, and the connecting interpolation rule, shown in Fig.1. Suppose that the refined area is $\bar{N}_x \times \bar{N}_y$ coarse cells.

In this paper, instead of embedding the fine grid system into the main coarse grid directly, the fine grid is first merged with the connecting interpolation rule, shown in Fig.1.

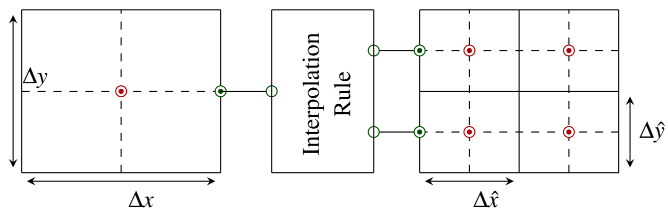

Figure 1. Connection between the coarse and fine grid for $r = 2$.

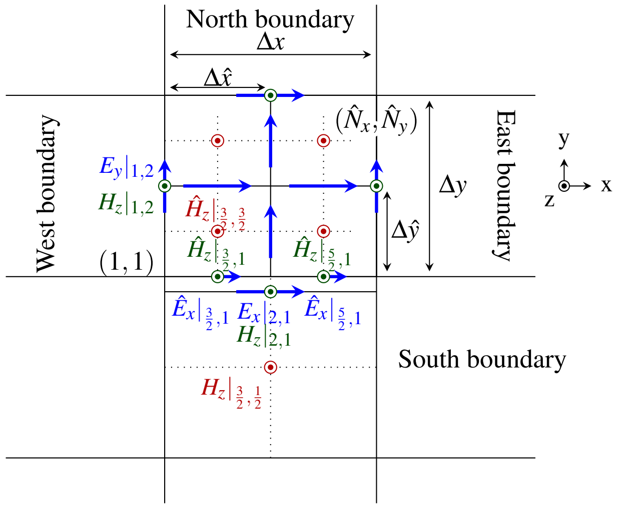

Figure 2. Graphical representation of the 2D multiscale scenario in Sec. 2.1, green denotes the introduced hanging variables.

2.1 Input Order Reduction Algorithm

Firstly, the fine grid system is analyzed separately. As described in [8], standard FDTD update equations are used for the nodes that are strictly located inside the fine region.

For the nodes on the boundaries, a modified Maxwell's equation is applied for the half step size instead of the full step size. For instance, the number of fine cells along the South boundary of the fine region is $\hat{N}_x = \bar{N}_x \times r$. There are $\hat{N}_x$ update equations along the south boundary of the fine grid

$$\begin{aligned}\Delta\hat{x}\frac{\Delta\hat{y}}{2}\left(\frac{\varepsilon_x}{\Delta t}+\frac{\sigma_x}{2}\right)\hat{E}_x\Big|^{n+1}_{i+\frac{1}{2},1} &= \\ \Delta\hat{x}\frac{\Delta\hat{y}}{2}\left(\frac{\varepsilon_x}{\Delta t}-\frac{\sigma_x}{2}\right)\hat{E}_x\Big|^{n}_{i+\frac{1}{2},1} & \\ +\Delta\hat{x}H_z\Big|^{n+\frac{1}{2}}_{i+\frac{1}{2},1+\frac{1}{2}}-\Delta\hat{x}H_z\Big|^{n+\frac{1}{2}}_{i+\frac{1}{2},1}, &\end{aligned} \tag{1}$$

where the introduced magnetic field $H_z|^{n+\frac{1}{2}}_{i+\frac{1}{2},1}$ on the boundary is used to replace the magnetic fields outside the fine region $H_z|^{n+\frac{1}{2}}_{i+\frac{1}{2},j-\frac{1}{2}}$. The boundary magnetic field are called the introduced hanging variables to update the boundary E_x nodes [8]. Similarly, the $\hat{E}^n_y$ on the West boundary is updated:

$$\begin{aligned}\Delta\hat{y}\frac{\Delta\hat{x}}{2}\left(\frac{\hat{\varepsilon}_y}{\Delta t}+\frac{\hat{\sigma}_y}{2}\right)\hat{E}_y\Big|^{n+1}_{1,j+\frac{1}{2}} &= \\ \Delta\hat{y}\frac{\Delta\hat{x}}{2}\left(\frac{\hat{\varepsilon}_y}{\Delta t}-\frac{\hat{\sigma}_y}{2}\right)\hat{E}_y\Big|^{n}_{1,j+\frac{1}{2}} & \\ +\Delta\hat{y}\hat{H}_z\Big|^{n+\frac{1}{2}}_{1,j+\frac{1}{2}}-\Delta\hat{y}\hat{H}_z\Big|^{n+\frac{1}{2}}_{1+\frac{1}{2},j+\frac{1}{2}}. &\end{aligned} \tag{2}$$

To combine the fine grid with the main coarse grid, a lossless interpolation rule among fields on the boundaries is used in [8]. A transformation matrix $\mathbf{T}$ is imposed to map the coarsely-sampled fields to the finely-sampled fields

$$\hat{\mathbf{y}}^n = \mathbf{T}\bar{\mathbf{y}}^n \qquad \forall n, \tag{3}$$

where

$$\mathbf{T} = \mathbf{I}_{2\bar{N}_x+2\bar{N}_y} \otimes \mathbf{T}_t\,. \tag{4}$$

In (4), $\mathbf{I}_{2\bar{N}_x+2\bar{N}_y}$ is an identity matrix and the subscript denotes the matrix size. $\mathbf{T}_t$ is a $1\times r$ vector containing 1 representing a field transition matrix between one coarse cell and its adjacent r fine cells. Symbol $\otimes$ is used to represent the Kronecker Product.

Meanwhile, a reciprocal principle is applied on the magnetic fields on the interface to maintain the stability

$$\bar{\mathbf{u}}^{n+\frac{1}{2}} = \frac{1}{r}\mathbf{T}^T\hat{\mathbf{u}}^{n+\frac{1}{2}} \qquad \forall n. \tag{5}$$

If we average all the $\hat{E}^n_y$ along the West boundary, an equal coarsely-sampled $E_y|^{n+1}_{1,2}$ update equation is generated

$$\begin{aligned}\Delta\hat{y}\frac{\Delta\hat{x}}{2}\left(\frac{\sum\hat{\varepsilon}_y}{r\Delta t}+\frac{\sum\hat{\sigma}_y}{2r}\right)\hat{E}_y\Big|^{n+1}_{1,j+\frac{1}{2}} &= \\ \Delta\hat{y}\frac{\Delta\hat{x}}{2}\left(\frac{\sum\hat{\varepsilon}_y}{r\Delta t}-\frac{\sum\hat{\sigma}_y}{2r}\right)\hat{E}_y\Big|^{n}_{1,j+\frac{1}{2}} & \\ +\frac{\Delta\hat{y}}{r}\sum\hat{H}_z\Big|^{n+\frac{1}{2}}_{1,j+\frac{1}{2}}-\frac{\Delta\hat{y}}{r}\sum\hat{H}_z\Big|^{n+\frac{1}{2}}_{1+\frac{1}{2},j+\frac{1}{2}}. &\end{aligned} \tag{6}$$

In (6), the average of permittivity and conductivity along the interface of the adjacent r fine cells can be written as

$$\frac{\sum\hat{\varepsilon}_y}{r} = \frac{\mathbf{T}_t\hat{\mathbf{D}}_{\varepsilon_y}\mathbf{T}_t'}{r} \approx \varepsilon_y\,, \frac{\sum\hat{\sigma}_y}{r} = \frac{\mathbf{T}_t\hat{\mathbf{D}}_{\sigma_y}\mathbf{T}_t'}{r} \approx \sigma_y\,, \tag{7}$$

where ε_y and σ_y stand for the permittivity and conductivity of the corresponding coarse cell along the interface.

The average of the introduced hanging variables is also equivalent to the hanging variable of the adjacent magnetic field of the coarse grid

$$\frac{1}{r}\sum\hat{H}_z\Big|^{n+\frac{1}{2}}_{1,j+\frac{1}{2}} = H_z\Big|^{n+\frac{1}{2}}_{1,j+\frac{1}{2}}. \tag{8}$$

Therefore, we can merge the connection subsystem and fine grid subsystem together by substituting (7) into (6)

$$\begin{aligned}\Delta\hat{y}\frac{\Delta\hat{x}}{2}\left(\frac{\varepsilon_y}{\Delta t}+\frac{\sigma_y}{2}\right)E_y\Big|^{n+1}_{1,j+\frac{1}{2}} &= \\ \Delta\hat{y}\frac{\Delta\hat{x}}{2}\left(\frac{\varepsilon_y}{\Delta t}-\frac{\sigma_y}{2}\right)E_y\Big|^{n}_{1,j+\frac{1}{2}} & \\ \Delta\hat{y}H_z\Big|^{n+\frac{1}{2}}_{1,j+\frac{1}{2}}-\frac{\Delta\hat{y}}{r}\sum\hat{H}_z\Big|^{n+\frac{1}{2}}_{1+\frac{1}{2},j+\frac{1}{2}}. &\end{aligned} \tag{9}$$

In (9), the introduced hanging variables of the fine grid system are replaced by the coarsely-sampled magnetic fields on the boundary. Then, we collect all the update equations on the edges like (9) into matrix form

$$\begin{bmatrix} r\bar{\mathbf{D}}_{l_x}\bar{\mathbf{D}}_{l'_y}\left(\frac{\bar{\mathbf{D}}_{\varepsilon x}}{\Delta t}+\frac{\bar{\mathbf{D}}_{\sigma x}}{2}\right) & \mathbf{0} \\ \mathbf{0} & r\bar{\mathbf{D}}_{l_y}\bar{\mathbf{D}}_{l'_x}\left(\frac{\bar{\mathbf{D}}_{\varepsilon y}}{\Delta t}+\frac{\bar{\mathbf{D}}_{\sigma y}}{2}\right) \end{bmatrix} \bar{\mathbf{E}}^{n+1}$$
$$= \begin{bmatrix} r\bar{\mathbf{D}}_{l_x}\bar{\mathbf{D}}_{l'_y}\left(\frac{\bar{\mathbf{D}}_{\varepsilon x}}{\Delta t}-\frac{\bar{\mathbf{D}}_{\sigma x}}{2}\right) & \mathbf{0} \\ \mathbf{0} & r\bar{\mathbf{D}}_{l_y}\bar{\mathbf{D}}_{l'_x}\left(\frac{\bar{\mathbf{D}}_{\varepsilon y}}{\Delta t}-\frac{\bar{\mathbf{D}}_{\sigma y}}{2}\right) \end{bmatrix} \bar{\mathbf{E}}^{n}$$
$$+\bar{\mathbf{M}}\hat{\mathbf{H}}_z^{n+\frac{1}{2}} + \begin{bmatrix} r\bar{\mathbf{D}}_{l_x}\bar{\mathbf{B}}_x & \mathbf{0} \\ \mathbf{0} & r\bar{\mathbf{D}}_{l_y}\bar{\mathbf{B}}_y \end{bmatrix} \mathbf{U}^{n+\frac{1}{2}}, \quad (10)$$

where

$$\bar{\mathbf{E}}^{n+1} = \begin{bmatrix} \mathbf{E}_x^{n+1} \\ \mathbf{E}_y^{n+1} \end{bmatrix}, \mathbf{U}^{n+\frac{1}{2}} = \begin{bmatrix} \bar{\mathbf{u}}_x^{n+\frac{1}{2}} \\ \bar{\mathbf{u}}_y^{n+\frac{1}{2}} \end{bmatrix}, \quad (11)$$

$$\bar{\mathbf{M}} = \begin{bmatrix} \bar{\mathbf{D}}_{l_x}\mathbf{W}_1^{\hat{N}_y}\otimes\mathbf{I}_{\bar{N}_x}\otimes\mathbf{T}_t & \mathbf{0} \\ -\bar{\mathbf{D}}_{l_x}\mathbf{W}_{\hat{N}_y}^{\hat{N}_y}\otimes\mathbf{I}_{\bar{N}_x}\otimes\mathbf{T}_t & \mathbf{0} \\ \mathbf{0} & -\bar{\mathbf{D}}_{l_y}\mathbf{I}_{\bar{N}_y}\otimes\mathbf{T}_t\otimes\mathbf{W}_1^{\hat{N}_x} \\ \mathbf{0} & \bar{\mathbf{D}}_{l_y}\mathbf{I}_{\bar{N}_y}\otimes\mathbf{T}_t\otimes\mathbf{W}_{\hat{N}_x}^{\hat{N}_x} \end{bmatrix}, \quad (12)$$

$$\bar{\mathbf{B}}_x = \begin{bmatrix} -\mathbf{I}_{\bar{N}_x} & \mathbf{0} \\ \mathbf{0} & \mathbf{I}_{\bar{N}_x} \end{bmatrix}. \quad (13)$$

$\bar{\mathbf{D}}_{l_x}$ and $\bar{\mathbf{D}}_{l_y}$ are diagonal matrices consisting of length of fine grid primary cell along x and y directions. $\bar{\mathbf{D}}_{l'_x}$ and $\bar{\mathbf{D}}_{l'_y}$ stand for the length of the fine grid secondary cell on the interface connecting the fine grid. $\bar{\mathbf{D}}_{\varepsilon_x}$, $\bar{\mathbf{D}}_{\varepsilon_y}$, $\bar{\mathbf{D}}_{\sigma_x}$ and $\bar{\mathbf{D}}_{\sigma_y}$ represent diagonal matrices corresponding to the permittivity and conductivity on the coarse grid interface adjacent the fine region. Matrix $\bar{\mathbf{M}}$ is the discrete derivative operator along x and y directions, which is imposed to update the boundary electric fields with the fine grid magnetic fields $\hat{\mathbf{H}}_z^{n+\frac{1}{2}}$. $\mathbf{W}_i^n$ denotes a $1\times n$ row vector with all zeros except ith column defined as 1. $\mathbf{I}_{\bar{N}_x}$ and $\mathbf{I}_{\bar{N}_y}$ are identity matrices. Diagonal matrices $\hat{\mathbf{B}}_x$ and $\hat{\mathbf{B}}_y$ contain -1 and $+1$ in accordance with the introduced coarsely-sampled magnetic fields on the boundaries

$$\bar{\mathbf{B}}_y = \begin{bmatrix} \mathbf{I}_{\bar{N}_y} & \mathbf{0} \\ \mathbf{0} & -\mathbf{I}_{\bar{N}_y} \end{bmatrix}. \quad (14)$$

In comparison to the inputs defined in [7], it indicates that the input number of the joint subsystem is reduced from $4r\times(\bar{N}_x+\bar{N}_y)$ to $4\times(\bar{N}_x+\bar{N}_y)$.

Reciprocally, the corresponding fine grid magnetic fields connecting the boundary are updated using the coarsely-sampled electric fields on the boundaries. Update equations of all fine grid magnetic field can be written as the following matrix form using reciprocity rule,

$$\frac{\hat{\mathbf{D}}_A\hat{\mathbf{D}}_\mu}{\Delta t}\hat{\mathbf{H}}_z^{n+\frac{1}{2}} = \frac{\hat{\mathbf{D}}_A\hat{\mathbf{D}}_\mu}{\Delta t}\hat{\mathbf{H}}_z^{n-\frac{1}{2}} - \bar{\mathbf{M}}\bar{\mathbf{E}}^n + \hat{\mathbf{G}}_y\hat{\mathbf{D}}_{l_x}\hat{\mathbf{E}}_x^n - \hat{\mathbf{G}}_x\hat{\mathbf{D}}_{l_y}\hat{\mathbf{E}}_y^n, \quad (15)$$

where diagonal matrix $\hat{\mathbf{D}}_A$ consists of the primary cell areas and $\hat{\mathbf{D}}_\mu$ is diagonal containing the average secondary grid permittivity.

2.2 Dynamical System Formulation

Then a new subsystem can be generated by collecting (10), (15) and update equations of all nodes that strictly fall completely inside the fine region. The ports of the new generated subsystem are based on number of coarsely-sampled nodes on the boundaries instead of the finely-sampled ones. The joint system of fine grid update equations and connection scheme can be described by the following discrete time system

$$(\bar{\mathbf{R}}+\bar{\mathbf{F}})\bar{\mathbf{x}}^{n+1} = (\bar{\mathbf{R}}-\bar{\mathbf{F}})\bar{\mathbf{x}}^{n}+\bar{\mathbf{B}}\mathbf{U}^{n+\frac{1}{2}}, \quad (16a)$$
$$\mathbf{Y}^{n+1} = \bar{\mathbf{L}}^T\bar{\mathbf{x}}^{n+1}. \quad (16b)$$

The unknown vector $\bar{\mathbf{x}}^{n+1}$ consists of $\bar{\mathbf{E}}^n, \hat{\mathbf{E}}_x^n$, $\hat{\mathbf{E}}_y^n$ and $\hat{\mathbf{H}}_z^n$, the size of which are denoted as $2(\bar{N}_x+\bar{N}_y)\times 1$, $\hat{N}_x(\hat{N}_y-1)\times 1$, $(\hat{N}_x-1)\hat{N}_y\times 1$ and $\hat{N}_x\hat{N}_y\times 1$, respectively. The input $\mathbf{U}^{n+\frac{1}{2}}$ of the dynamical system contains the coarsely-sampled magnetic hanging variables on the North, South, West and East boundaries of the fine region $\mathbf{H}_S^{n+\frac{1}{2}}$, $\mathbf{H}_N^{n+\frac{1}{2}}$, $\mathbf{H}_W^{n+\frac{1}{2}}$, $\mathbf{H}_E^{n+\frac{1}{2}}$. The output $\mathbf{Y}^{n+1}$ contains the electric fields sampled at the same nodes as the inputs, which are denoted as $\mathbf{E}_S^n$, $\mathbf{E}_N^n$, $\mathbf{E}_W^n$, $\mathbf{E}_E^n$.

Therefore, it is evident that the number of inputs of the passive system (16a)-(16b) has been reduced through the proposed input reduction scheme compared with the one in [7].

2.3 Reduce Order Modeling

As described in [7], the application of model order reduction can greatly reduce the size of the dynamical system. Similarly, the method of SPRIM [9] is applied on the joint subsystem (16a) and (16b). A condensed system model is obtained as discussed in [7]

$$(\tilde{\mathbf{R}}+\tilde{\mathbf{F}})\tilde{\mathbf{x}}^{n+1} = (\tilde{\mathbf{R}}-\tilde{\mathbf{F}})\tilde{\mathbf{x}}^{n}+\tilde{\mathbf{B}}\mathbf{U}^{n+\frac{1}{2}}, \quad (17a)$$
$$\mathbf{Y}^{n+1} = \tilde{\mathbf{L}}^T\tilde{\mathbf{x}}^{n+1}, \quad (17b)$$

where the size of the generated reduced model (17a)-(17b) is r times smaller compared to the size of the reduced model in [7] with maintained accuracy, which will further significantly reduce the computational cost. Moreover, through the technique of CFL limit extension, we can also prove that as long as the reduced model remains to be dissipative under a larger time step, the entire system is guaranteed to be stable with a larger time step beyond the CFL limit of the find grid. In this way, the proposed method maintains the explicit characters of FDTD at a larger CFL limit with guaranteed stability.

3 Numerical Results

We apply the proposed algorithm to a human head exposure test, to investigate the radiation exposure of human head with the existence of an antenna. The setup of the test is shown in Fig. 3 [8]. A simulation domain

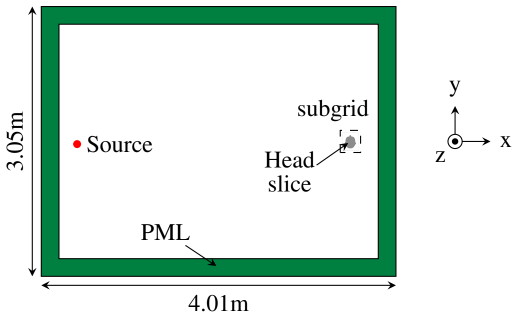

Figure 3. Layout of the human head exposure test [8], the head slice is in the dashed line area.

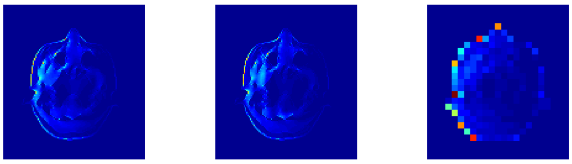

(a) All-fine (b) Proposed method (c) All-coarse

Figure 4. SAR maps of Sec. 3 with an all-fine, an all-coarse mesh and the proposed method for $r = 5$.

is 4.01 m $\times$ 3.05 m terminated with 20 cm-thick perfect matched layer on four sides. A 900 MHz sinusoidal source was used to excite the structure at the left side of the domain and the cross-section of human head slice was at the other side. The fine grid resolution of the dashed line area was set to 2 mm and the coarse grid cell size was set to 1 cm. The time step for an all-fine FDTD and an all-coarse FDTD is set to be 0.99 times their own CFL limit. The CFL number for the proposed method is 3.96. Specific absorption rate (SAR) was used to evaluate the radiation exposure. The SAR maps for an all-fine FDTD, an all-coarse FDTD and the proposed method are compared in Fig. 4. The results indicates that the proposed method is in good consistency with the reference results, an all-fine FDTD. Moreover, Table 1 shows the execution time and percent error of SAR corresponding to an all-fine FDTD. The proposed method achieves a 104.2X times speed-up with respect to all-fine FDTD simulation with error rate -3.38%.

Table 1. Execution time for human exposure test.

Method	Runtime	Speed-up	Error
All-fine grid	14,594 s	-	-
All-coarse grid	62 s	-	60.1%
Subgridding	357 s	40.1X	-3.1%
Proposed method	140 s	104.2X	-3.38%

4 Conclusion

In conclusion, our research successfully demonstrates the efficiency of an innovative FDTD subgridding algorithm, which incorporates model order reduction adaptable to arbitrary grid ratios. This approach significantly mitigates the computational challenges traditionally associated with FDTD methods, especially in scenarios requiring high spatial resolution. The algorithm not only ensures computational accuracy but also substantially reduces computational resources, proving its versatility across various complex electromagnetic simulation scenarios. This advancement not only addresses previous limitations in the field but also opens avenues for more efficient, accurate, and scalable electromagnetic modeling, paving the way for future research and applications in this domain.

References

[1] S. D. Gedney, *Introduction to the Finite-Difference Time-Domain (FDTD) method for electromagnetics*, 1st ed. San Rafael, CA: Morgan & Claypool Publishers, 2011.

[2] M. Okoniewski, E. Okoniewska, and M. Stuchly, “Three-dimensional subgridding algorithm for FDTD,” *IEEE Trans. Antennas Propag.*, vol. 45, no. 3, pp. 422–429, 1997.

[3] K. Xiao, D. J. Pommerenke, and J. L. Drewniak, “A three-dimensional FDTD subgridding algorithm with separated temporal and spatial interfaces and related stability analysis,” *IEEE Trans. Antennas Propag.*, vol. 55, no. 7, pp. 1981–1990, 2007.

[4] L. Kulas and M. Mrozowski, “Reduced order models of refined Yee’s cells,” *IEEE Microw. Wireless Compon. Lett.*, vol. 13, no. 4, pp. 164–166, 2003.

[5] X. Li and P. Triverio, “Stable FDTD simulations with subgridding at the time step of the coarse grid: a model order reduction approach,” in *IEEE MTT-S Int. Conf. on Numerical Electromagnetic and Multiphysics Modeling and Optimization*, Ottawa, Canada, August 11–14 2015.

[6] A. Zadehgol, “An impedance transfer function formulation for reduced-order macromodels of subgridded regions in FDTD,” *IEEE Trans. Antennas Propag.*, vol. 65, no. 1, pp. 401–404, Jan 2017.

[7] X. Zhang, F. Bekmambetova, and P. Triverio, “A stable FDTD method with embedded reduced-order models,” *IEEE Trans. Antennas Propag.*, vol. 66, no. 2, pp. 827–837, 2018.

[8] F. Bekmambetova, X. Zhang, and P. Triverio, “A dissipative systems theory for FDTD with application to stability analysis and subgridding,” *IEEE Trans. Antennas Propag.*, vol. 65, no. 2, pp. 751–762, 2017.

[9] R. W. Freund, “SPRIM: Structure-preserving reduced-order interconnect macromodeling,” in *Proceedings of the 2004 IEEE/ACM International Conference on Computer-aided Design*, Washington, DC, USA, 2004.